PHASE I REPORT

DATE: July 27, 2009

Project Title: Seabed Scour and Buried-Pipeline Deformation Due to Ice Ridges

MMS Project: 601 **TO Number:** AC12418

Project PI: J.L. Tassoulas

COTR: M. Else

Phase I Completion Date: 8/31/2008

Introduction

Scour of the Arctic seabed has long been identified as a potentially catastrophic environmental hazard for marine pipelines. A moving ice ridge can scour the soil and destroy a pipeline in its path. In contrast to "upheaval buckling," another phenomenon of grave concern, in which, the relevant (thermal) load is longitudinal, the effects of ice-ridge scouring are associated with lateral loads on pipelines. Also, while upheaval buckling can be prevented by means of heavy (rock or other material) cover placed on top of the pipelines, protection from scouring typically relies on sufficient pipeline-burial depth, or adequate trenching and trench-backfilling requirements.

There is general agreement that the ice-ridge scour depth along with the pipeline burial depth (both measured from the top of the soil) can be used in evaluating the outcome of ridge-soil-pipeline interaction. If the scour and burial depths are about the same, there is little doubt that pipeline integrity will be compromised. At the other extreme, if the burial depth is sufficiently greater than the scour depth, the pipeline is not expected to undergo any significant deformation. Survival of the pipeline can then be assumed. The minimum "sufficient" burial depth has not been firmly established but values as low as three times the scour depth have appeared in the literature (Yang and Poorooshasb 1997). In the intermediate range (burial depth equal to a few scour depths), it appears reasonable to expect that the pipeline can be designed so that survival can be ensured, perhaps, with some permanent deformation. Such an outcome may be preferable to the costlier alternative of specifying a greater depth of burial. That these three ranges (Palmer 1997) are meaningful for design purposes has been demonstrated through laboratory and field observations (Woodworth-Lynas 1992, Paulin 1992, Lach et al. 1993, Yang et al. 1994, Clark et al. 1994) of substantial "sub-scour" soil deformation (at a few scour depths below the top of the soil). However, it is important to keep in mind that sub-scour soil deformation can only serve as an indicator of the loads likely to be experienced by the pipeline. Only through a study of the complete ridge-soil-pipeline system can the actual levels of stress and strain in the pipeline be ascertained. A complete system study is proposed herein.

Ice ridges move at speeds of about 0.1 m/s and scour the seabed at low "attack" angles, usually smaller than 30°, and various lengths and widths of the "keel." At steady state, the scour depth is, in general, a function of the ridge geometry, speed, vertical stiffness (resulting from buoyancy) and the soil properties (near the surface of the seabed). The scoured soil is placed, partially, on berms on the sides of the ridge path. It is the rest of the scoured soil that is pressed downwards and sheared (and pushed) forwards. In turn, downward pressure and shear at the keel appear to produce upward soil movement ahead of the keel. It is the balance of soil placed on berms, pressed, sheared and displaced, along with the buoyancy and kinematics of the ice ridge that sets the stage for ice scouring of the seabed. In the presence of a pipeline buried within a few scour depths, soil deformation amounts to lateral load on the pipeline that can result in loss of integrity or permanent deformation. The three-dimensional nature of the phenomenon is quite clear and accounts for a relatively concentrated lateral load (over a few pipeline diameters) on the pipeline and the formation of berms. In fact, it is the absence of the latter features (berms) from "two-dimensional" centrifuge tests and corresponding computational simulations that limit the realism of studies to date. Nevertheless, two-dimensional investigations, experimental or computational, are useful in our quest for better understanding of the phenomenon. Effectively, they provide insight in seabed scour by an infinitely-wide ice keel.

Although conceivable, it appears very unlikely that "failure" of the scouring keel can occur as an ice ridge moves along the seabed, as the normal and shearing stresses are low. This is believed to be the case with multiyear and first-year ridges (Kovacs and Mellor 1974). For the same reason, it is reasonable to neglect the deformability of the ice ridge. Indeed, in experimental and computational studies to date, the ice ridge has been represented as a rigid body.

Quite extensive centrifuge tests of ridge-soil systems have already been conducted (Winsor and Parsons 1997, Hurley and Phillips 1999, Schoonbeek and Allersma 2006), many with support from the Minerals Management Service. The results are available for interpretation and understanding of various facets of the phenomenon such as sub-scour deformation, berms and multiple (or repeated) scouring, the influence of soil behavior (clay vs. sand), layered seabed as well as the effects of parameters such as keel width, length and attack angle. Also, the test results can be used toward calibration and verification of computational models.

As mentioned earlier, experiments and computations to date have focused largely on sub-scour deformation as an indicator of pipeline vulnerability. Essentially, such investigations have explored behavioral features of *ridge-soil* systems. For example, Konuk and Gracie (2004) used the finite-element method along with an Arbitrary Lagrangian-Eulerian formulation and a soil-plasticity cap model to examine seabed scour. In recent years, limited studies of *ridge-soil-pipeline* systems have been undertaken. Konuk and Yu (2007) reported results of finite-element computations for complete ridge-soil-pipeline systems by an Arbitrary Lagrangian-Eulerian formulation (and a cap model of elastoplastic soil behavior). Nobahar et al. (2007) developed and applied an adaptive finite-element model of ridge-soil-pipeline systems on the basis of a Lagrangian formulation. The latter development included a representation of soil-pipeline interaction by means of a Winkler beam on a nonlinear (soil) foundation away from the

scour. In the present Project, we explore an approach toward ridge-soil-pipeline modeling within the framework of Computational Fluid Dynamics (CFD). Effectively, our CFD approach relies on an Eulerian formulation of the "flow" of soil as a viscous fluid. We believe that this novel approach and the treatment of soil as a viscous fluid are in line with the extensive soil rearrangements that occur during scour of the seabed by ice ridges.

Although the ultimate goal of our Project is to develop CFD models of complete ridge-soil-pipeline systems, our objective in this Phase I is to demonstrate the viability of our procedure in ridge-soil system analysis. In the present Report, we will describe the steps involved in CFD modeling of ridge-soil systems and proceed to examine the results of simulations. We will not consider soil-pipeline interaction in Phase I of the Project. However, we will report estimates of the maximum bending stress in buried pipelines due to seabed scour in the absence of interaction.

Computational Procedure

We shall first describe the ingredients of our CFD procedure for ridge-soil system analysis. The development of our procedure was carried out using FLUENT (http://www.fluent.com), a general-purpose, commercially-available, CFD code. When dealing with ridge-soil systems, it is best to compute the system response at steady state. Such FLUENT computations can be carried out in a straightforward manner.

Mesh

We use meshes of tetrahedral cells in the domain of interest that includes soil and water with the ice ridge represented by a rigid body and boundaries placed sufficiently far from the ridge at top, bottom, front and rear. Examples will be shown below. The meshes must be particularly fine in the region of greatest interest, up to some height above and down to some depth below the base of the ice ridge. Above the base, the fine mesh is necessary in order to capture the soil-water interface, especially, the soil mound ahead of the ridge. On the other hand, a fine mesh below the base will permit accurate estimation of soil pressure and shear for the calculation of distributed loads on buried pipelines. We use the "volume-of-fluid" model available in FLUENT for multiphase (soil-water) flow. The base of the ice ridge is positioned at any specified scour depth below the sea bottom.

Soil Model

Of key significance in the present study, is the simplified treatment of the soil as a viscous fluid, represented in FLUENT by a Herschel-Bulkley model. The most important parameter of the model is the yield shear stress, τ_0, representing the ("undrained") soil (shear) strength. As long as the shear strain rate, $\dot{\gamma}$, remains below the yield shear strain (a parameter of the model), $\dot{\gamma}_0$, the shear stress, τ, increases linearly with shear strain rate:

$$\tau = \mu_0 \dot{\gamma} \tag{1}$$

μ_0 being the yield viscosity. The remaining two parameters of the model describe the behavior at levels of shear strain rate exceeding $\dot{\gamma}_0$:

$$\tau = \tau_0 + \kappa(\dot{\gamma}^n - \dot{\gamma}_0{}^n) \quad (2)$$

In Equation 2, n and κ are the power-law index and the consistency index, respectively. For any given τ_0 and $\dot{\gamma}_0$, the power-law index and the consistency index can be adjusted so as to represent the effects of shear strain rate on viscous behavior. An example of a shear stress vs. shear strain rate relationship specified by the Herschel-Bulkley model is shown (in normalized form: τ/τ_0 vs. $\dot{\gamma}/\dot{\gamma}_0$) in Figure 1. In fact, the curve of Figure 1 corresponds to the clayey soil considered in the CFD simulations to be reported below. It is worth mentioning that an alternative simpler version of Equation 2 can be written as:

$$\tau = \tau_0[1 + \lambda \log_{10}(\dot{\gamma}/\dot{\gamma}_0)] \quad (3)$$

This latter equation uses a single parameter ("strain-rate-effect" parameter), λ, that indicates the dimensionless increase in shear stress (increase divided by the yield shear stress) with tenfold increase in shear strain rate beyond $\dot{\gamma}_0$. It is straightforward to introduce Equations 1 and 3 as replacements of 1 and 2 in FLUENT (user-defined functions) for the purpose of describing soil behavior as a viscous fluid. In fact, another recent study by Raie (2009) applied Equations 1 and 3 to simulations of torpedo-anchor installation in clayey soils. However, in the present study, the Herschel-Bulkley model as implemented in FLUENT (Equations 1 and 2) was used. The curve of Figure 1 corresponds to $\lambda = 0.1$.

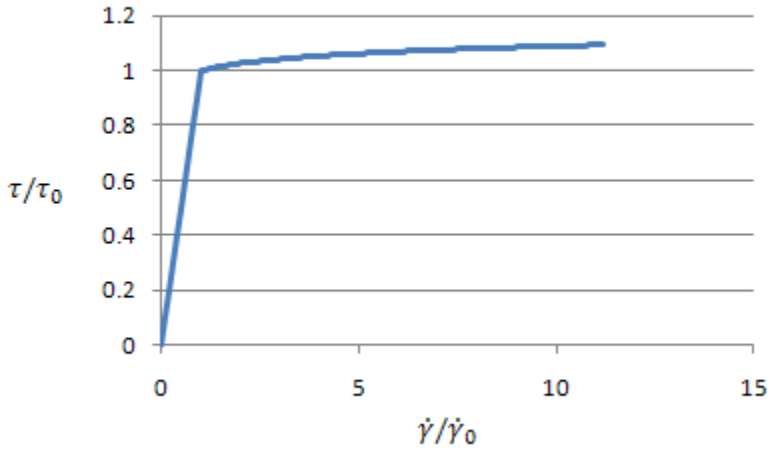

Figure 1: Shear stress vs. shear strain rate according to the Herschel-Bulkley model. In the present study, the power-law index and the consistency index are adjusted so that the model produces a *10%* increase in shear stress with a tenfold increase in shear strain rate (at rates higher than the yield shear strain rate). Such viscous behavior is fairly typical of clayey soils.

Pressure and Shear Distributions

After the steady state of the ridge-soil system is determined, we proceed to extract the pressure and shear distributions on cylindrical surfaces corresponding to fictitious

pipelines buried in the soil. A drawing of the array of pipes will be provided below as we discuss the simulations that we carried out. By integration of the pressure and shear distributions over the exterior surface of any pipe, we obtain the distribution of horizontal and vertical forces on each pipeline. For this purpose, we use the values of pressure and shear furnished by FLUENT at numerous azimuthal and longitudinal locations along each pipeline.

Results

We will present and discuss results of the FLUENT simulations of ridge-soil systems we have completed to date. A rigid ridge shaped as a truncated cone was assumed in all simulations. Also, the seabed was represented by a homogeneous layer of viscous fluid and the scour depth was kept constant. Only the effects of mesh fineness and ice-ridge speed were varied were examined.

Cases Analyzed

Table 1 summarizes the cases analyzed. In Cases 1, 4 and 5, fine, medium and coarse meshes were used, respectively, but all parameters of the ridge-soil system were kept the same. On the other hand, in Cases 1, 2 and 3, the fine mesh was used but the ridge speed was varied: *0.2 m/s* in Case 1, *0.5 m/s* in Case 2 and *1.0 m/s* in Case 3. In all cases, the scour depth was set at *1.0 m* and the soil yield stress at *25 kPa*. The pipeline exterior diameter was taken equal to *0.61 m (24 in)* and the nominal wall thickness *25.4 mm (1 in)*. The ice ridge was represented by a rigid truncated cone with base diameter of 10 m and attack angle of 30.47° (with respect to the horizontal direction). The base diameter and attack angle are the same as those in the study by Nobahar et al. (2007). Also, we assumed that the higher soil (by 1 m) was engaged by the ridge at the beginning of the analysis. Then, step-by-step, we continue the FLUENT computations until a steady state is reached.

Case	Mesh	Ridge Speed
1	*Fine*	*0.2 m/s*
2	*Fine*	*0.5 m/s*
3	*Fine*	*1.0 m/s*
4	*Medium*	*0.2 m/s*
5	*Coarse*	*0.2 m/s*

Table 1: Cases Analyzed

Mesh Fineness

The fine, medium and coarse meshes are depicted in Figures 2-5. In the fine mesh, we use 642247 tetrahedral cells varying in dimension from *0.3 m* to *1.0 m*. The medium and coarse meshes contain, respectively, 349094 tetrahedral cells (with sizes from *0.7 m* to *1.0 m*) and 296853 tetrahedral cells (with sizes from *1.0 m* to *2.0 m*). Of these three meshes, only the fine mesh has cell size smaller than the pipeline diameter (*0.61 m*). We had intended to examine even finer meshes for the purpose of a convergence study. However, the fine mesh turned out to be the finest allowed by our computational resources (desktop PC) in the course of Phase I of the Project.

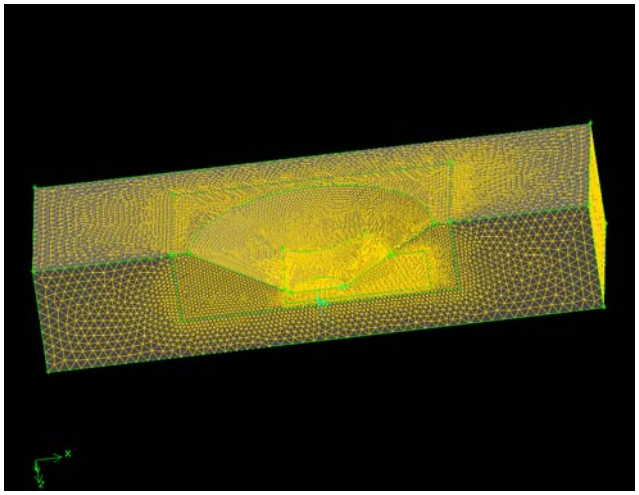

Figure 2: Fine mesh used in the FLUENT computations (Cases 1, 2 and 3).

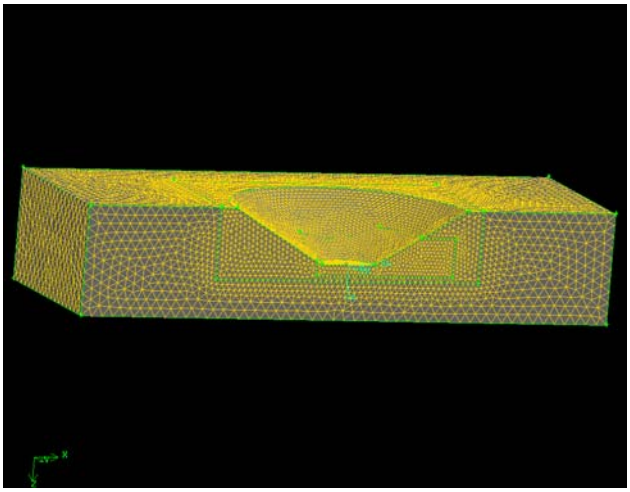

Figure 3: Medium mesh used in the FLUENT computations (Case 4).

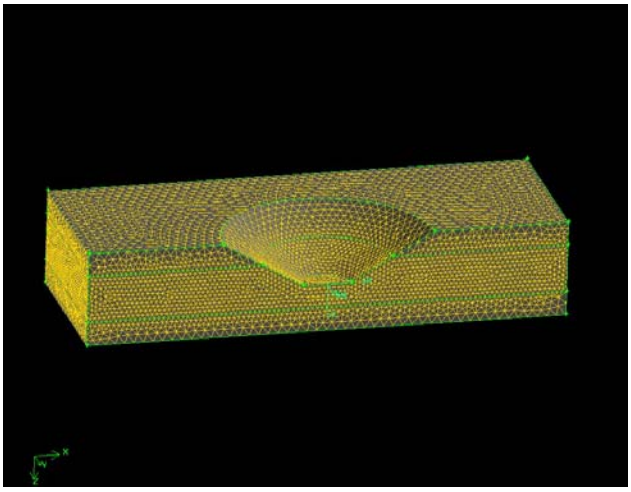

Figure 4: Coarse mesh used in the FLUENT computations (Case 5).

Soil

As mentioned above, we use a Herschel-Bulkley model for the description of soil behavior (Equations 1-2). The yield shear stress, τ_0, is set at *25 kPa* while the rest of the parameters, μ_0, κ and n, were taken equal to, respectively, *1037345*, *32578* and *0.0321*, in consistent units (*Pa, m, s*). The shear stress vs. shear strain rate curve is shown in Figure 1. At shear-strain-rate levels higher than $\dot{\gamma}_0$, the Herschel-Bulkley model with the selected parameter values provides (approximately) a *10%* increase in shear stress for a tenfold increase in shear strain rate. It is, therefore, equivalent to using Equation 3 with $\lambda = 0.1$ instead of Equation 2.

Buried Pipelines

Shown in Figure 5 are the locations of "fictitious" buried pipelines for which we estimate the maximum bending stress due to horizontal and vertical distributed loads resulting from the pressure and shear exerted by the soil. The latter data are extracted from the FLUENT-computed stead state at longitudinal stations (cross sections) spaced at *1 m* along each pipeline. For each longitudinal station, the values of pressure and shear are retrieved at 16 azimuthal stations (see Figure 6).

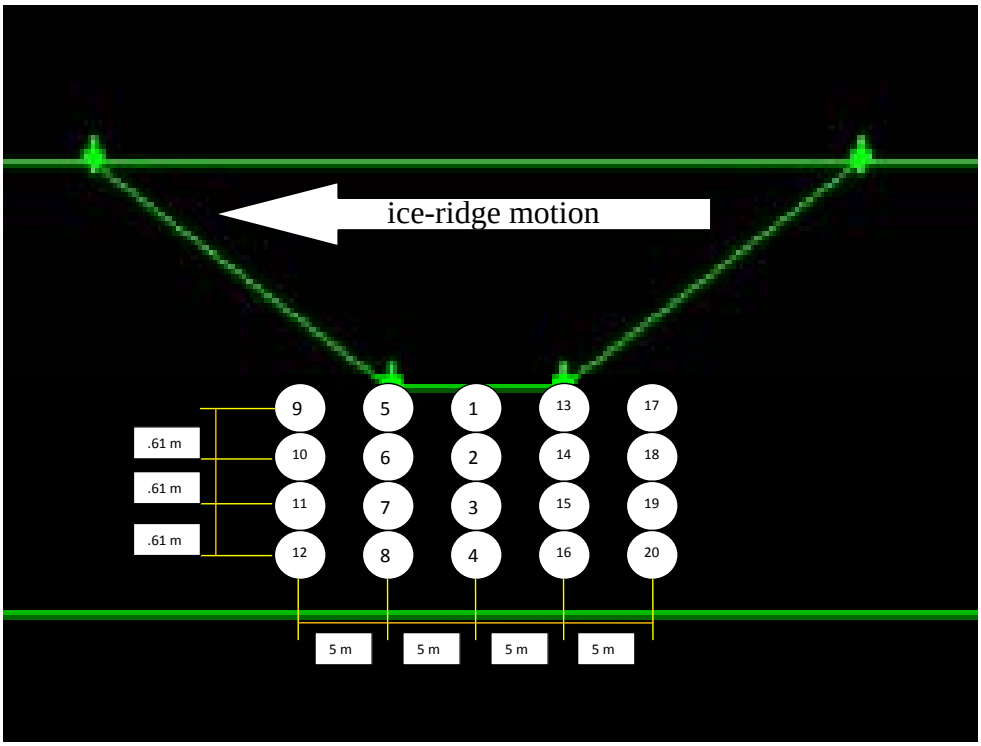

Figure 5: Array of cylindrical surfaces ("pipelines") on which soil pressure and shear distributions are extracted from the FLUENT steady-state computations.

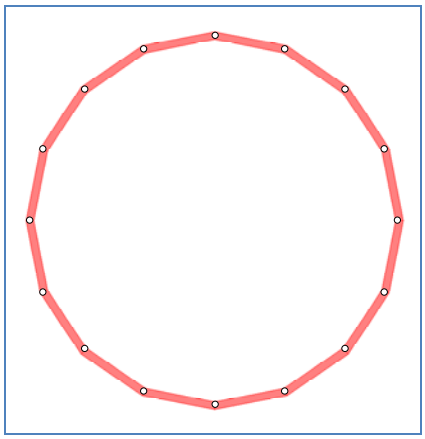

Figure 6: Points on each longitudinal station (pipeline cross-section) where soil pressure and shear are retrieved from the FLUENT computations.

Seabed Scour

Figures 7-9 depict the soil profile (in red) on a the vertical plane that contains the axis of ridge symmetry and parallel to the direction of motion. Particularly notable is the soil mound that forms at the front of the ice ridge. The height of the mound is a few times the scour depth. Comparing the three figures, it can be concluded that the mound height increases with increasing ridge speed. Since the higher ridge speed implies greater shear strain rates and, in turn, the Herschel-Bulkley model produces an increased level of shear by which the ridge "drags" more soil onto the mound. This effect is most visible in Figure 9, for the highest ridge speed considered (*1.0 m/s*). Indeed, the soil profile in Figure 9 includes a relatively steep edge at the front of the mound. While our computational evidence is not extensive enough to warrant firm conclusions, it appears that the increased mound size may be thought of as equivalent to reduced scour depth since the ridge front effectively moves soil to the top of the mound thus leaving less of the seabed to be scoured by the ridge base. The increase in mound height with faster-moving ridges is certainly a consequence of the viscous behavior (strain-rate dependence) described by the Herschel-Bulkley model that we adopted for the soil. Such behavior has not been included and, accordingly, no ridge-speed effects have been noted in other recent studies. We should add that, although the Herschel-Bulkley model parameter values we specified are typical of clayey soils, the selection of realistic parameter values for seabeds in the Arctic environment must be reconsidered in future work.

The soil profiles computed by the fine, medium and coarse meshes for the lowest ridge speed (*0.2 m/s*) are shown in Figure 10. Most remarkable is the appearance of water or soil-water mixture "pockets" along the ridge-soil interface when using the medium ot coarse meshes. One such "pocket" appears below the ridge front when using the medium mesh (Figure 10b). Several such "pockets" appear below the ridge front and base when using the coarse mesh (Figure 10c). No "pockets" of soil-water mixture are found below the ridge front or base when using the fine mesh. These "pockets" lead to reduced shear applied on the soil by the ridge. At this time, our limited computational experience indicates that these "pockets" are only mesh-dependent artifacts. In fact, one the basis of the appearance of these pockets, it seems reasonable to dismiss both the medium and coarse meshes as not fine enough.

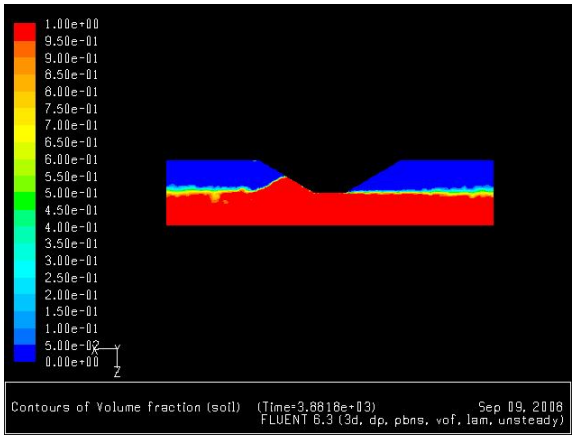

Figure 7: Snapshot of the ridge-soil system at steady state in Case 1 (*fine mesh;* ridge speed: *0.2 m/s*).

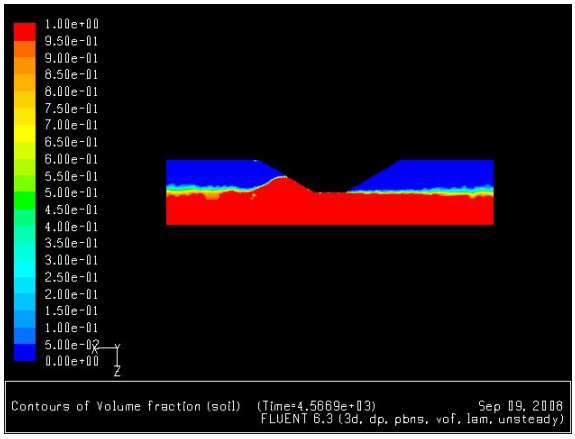

Figure 8: Snapshot of the ridge-soil system at steady state in Case 2 (*fine mesh;* ridge speed: *0.5 m/s*).

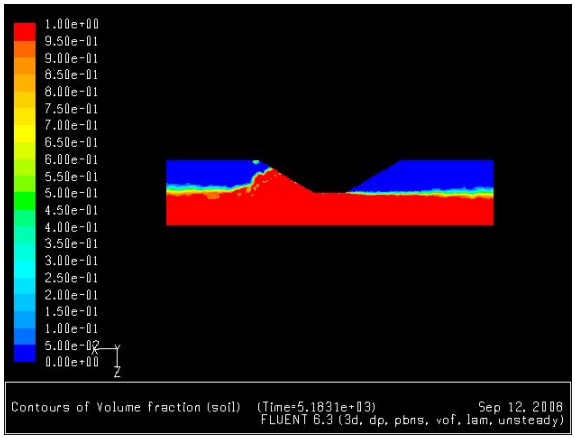

(a) ridge speed: *1.0 m/s*

Figure 9: Snapshot of the ridge-soil system at steady state in Case 3 (*fine mesh;* ridge speed: *1.0 m/s*).

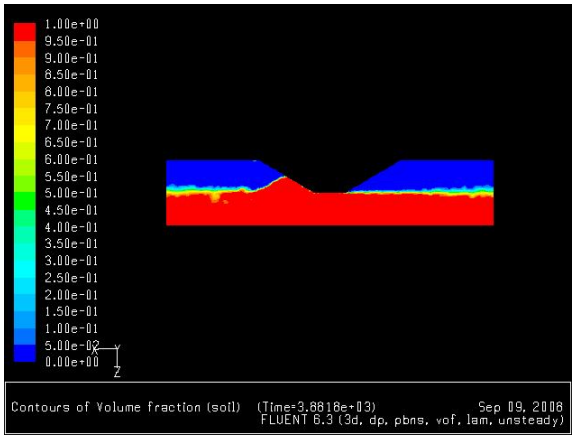

(a) fine mesh

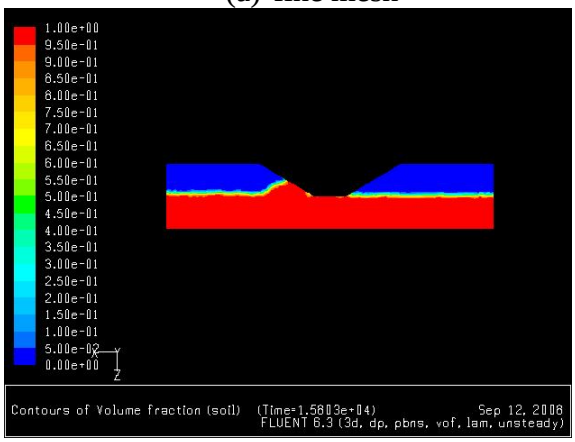

(b) medium mesh

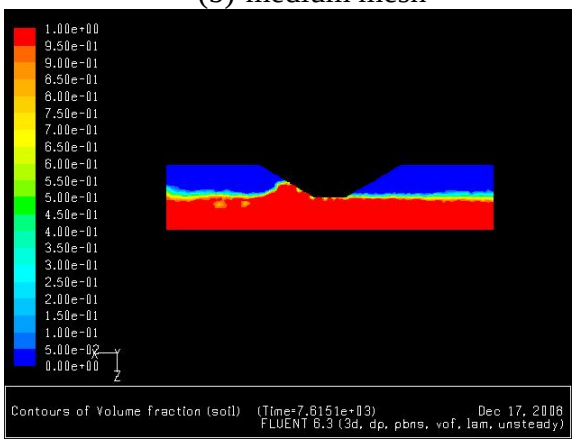

(c) coarse mesh

Figure 10: Snapshots of the ridge-soil system at steady state computed using (a) the *fine mesh* (Case 1), (b) the *medium mesh* (Case 4) and (c) the *coarse mesh* (Case 5).

Pipelines

The horizontal and vertical distributed loads on selected pipelines are shown in Figures 11 and 12. All pipelines are *70-m* long, symmetrically located with respect to the moving ridge. The distributions plotted in the figures are over half of each pipeline. As

mentioned earlier, these distributions are obtained by integration of pressure and shear exerted by the soil on the exterior surface of the fictitious pipelines. Clearly, only pipes 5, 1 and 13 are subjected to any appreciable loads. Referring to Figure 5, all three of these pipes are immediately under the ridge base, pipe 5 being at the front, pipe 1 at the center and pipe 13 at the rear. The forces in the figures are those corresponding to slowest ridge considered (Case 1; ridge speed: *0.2 m/s*). Pipe 1 (the central one) has the highest horizontal load and Pipe 13 the highest vertical load in this case.

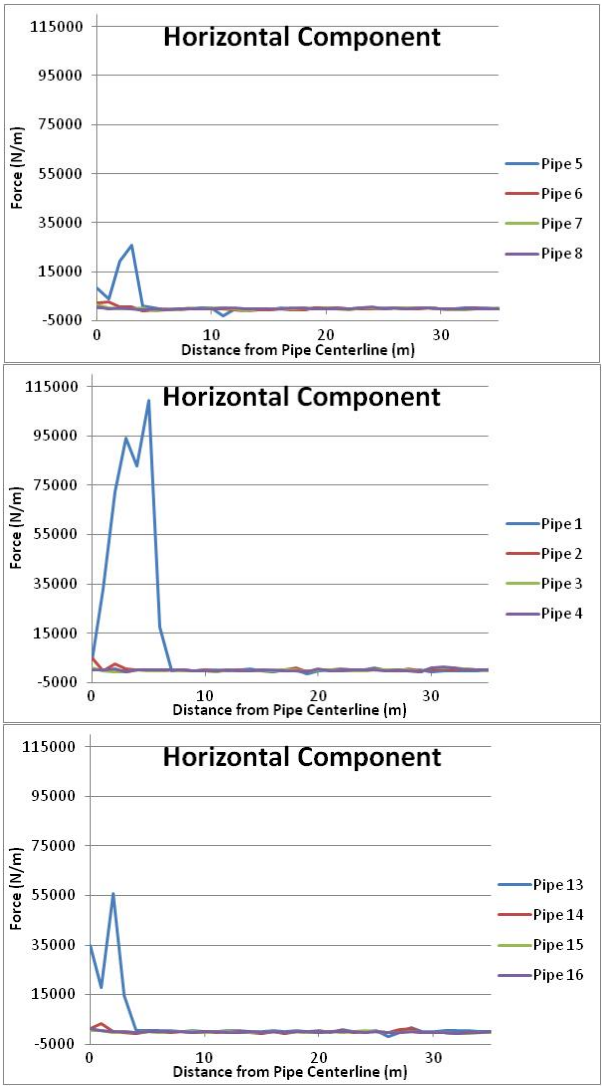

Figure 11: Distributions of horizontal loads on pipes under the ice ridge in Case 1 (*fine mesh;* ridge speed: *0.2 m/s*).

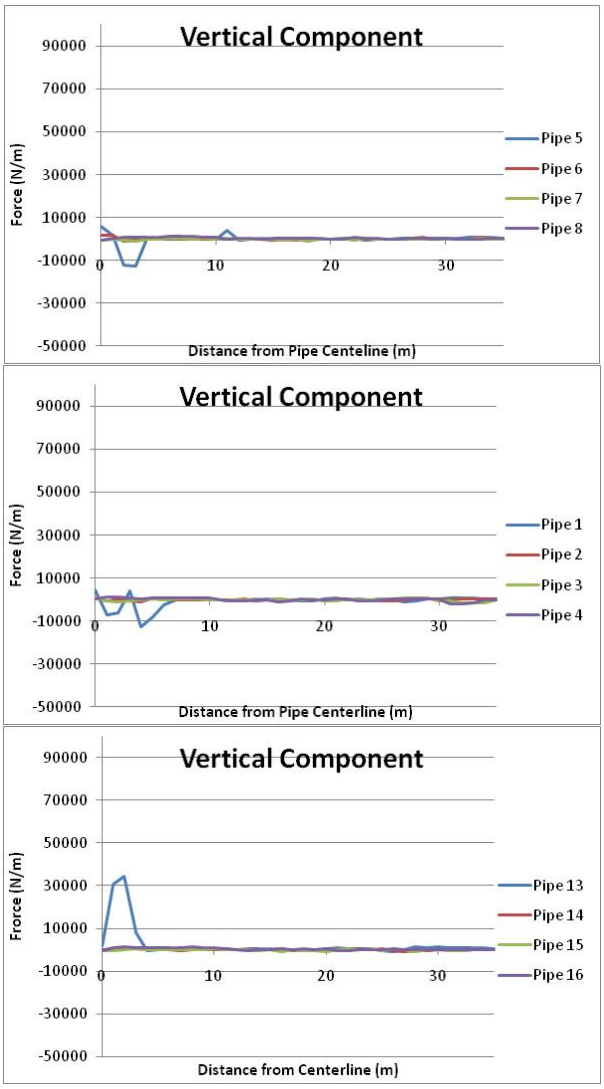

Figure 12: Distributions of vertical loads on pipes under the ice ridge in Case 1 (*fine mesh;* ridge speed: *0.2 m/s*).

Next, we apply the computed distributions of horizontal and vertical loads on beam models of the pipelines and proceed to obtain the maximum bending stress in each case. We are not considering soil-pipe interaction in the present study. So, the calculated maximum bending stress values should be viewed as rough estimates. Tables 2-6 summarize the estimated maximum bending stress in Pipes 5, 1 and 13 for each of the cases analyzed (Table 1). Estimates are provided for simple and fixed supports at the ends of the *70-m* long pipes. The stress estimates are normalized by the yield stress of a commonly used pipeline material. Tables 5 and 6 correspond to computations using medium and coarse meshes. We have already commented above that in these cases, "pockets" of soil-water mixture appear along the ridge-soil interface. These "pockets" reduce the shear exerted by the ridge and, expectedly, the resulting estimated stress in the buried pipelines is lower. Our understanding at this time is that the medium and coarse meshes are insufficiently fine. Therefore, the results for Cases 4 and 5 are shown only for the sake of completeness.

Pipe	Stress (psi)		Stress/F_y	
	Simply Supported Beam	Fixed Beam	Simply Supported Beam	Fixed Beam
Pipe 5	14862.	8415.	0.29	0.16
Pipe 1	104640.	63981.	2.01	1.23
Pipe 13	31407.	17387.	0.60	0.33

Table 2: Maximum bending stress (F_y = 52000 psi) in each of the (fictitious) pipelines located in the top row (see Figure 5) computed in Case 1 (fine mesh; ridge speed: *0.2 m/s*).

Pipe	Stress (psi)		Stress/F_y	
	Simply Supported Beam	Fixed Beam	Simply Supported Beam	Fixed Beam
Pipe 5	18248.	10770.	0.35	0.21
Pipe 1	81794.	52583.	1.57	1.01
Pipe 13	45296.	25858.	0.87	0.50

Table 3: Maximum bending stress (F_y = 52000 psi) in each of the (fictitious) pipelines located in the top row (see Figure 5) computed in Case 2 (fine mesh; ridge speed: *0.5 m/s*).

Pipe	Stress (psi)		Stress/F_y	
	Simply Supported Beam	Fixed Beam	Simply Supported Beam	Fixed Beam
Pipe 5	3294.	1977.	0.06	0.04
Pipe 1	36249.	24337.	0.70	0.47
Pipe 13	52959.	30467.	1.02	0.59

Table 4 Maximum bending stress (F_y = 52000 psi) in each of the (fictitious) pipelines located in the top row (see Figure 5) computed in Case 3 (fine mesh; ridge speed: *1.0 m/s*).

Although the maximum bending-stress levels in Tables 2-4 are quite high, it should be kept in mind that all three of the pipes (Pipes 5, 1 and 13) for which we report results are "located" immediately below the ridge base. The next row of pipelines has a soil cover of a pipeline diameter (*0.61 m*) and very low maximum bending stresses. An interesting trend shown in Tables 2-4 is that speedier ridges (Tables 3 and 4) produce lower maximum stress levels. This outcome is consistent with the observation above (see the subsection on *Seabed Scour*) that the soil-mound size increases with increasing ridge speed and the effect appears to be "equivalent" to a reduced scour depth. Another trend associated with higher ridge speeds is that Pipe 13 (the pipe located under the ridge base at the rear) is stressed at a higher level as the speed increases from *0.2 m/s* to *0.5 m/s* (Case 1 to Case 2) and then becomes the most stressed of the pipes as the speed is increased to *1.0 m/s* (Case 3).

Pipe	Stress (psi)		Stress/F_y	
	Simply Supported Beam	**Fixed Beam**	**Simply Supported Beam**	**Fixed Beam**
Pipe 5	4316.	2616.	0.08	0.05
Pipe 1	28674.	17184.	0.55	0.33
Pipe 13	5140.	3162.	0.10	0.06

Table 5: Maximum bending stress (F_y = 52000 psi) in each of the (fictitious) pipelines located in the top row (see Figure 5) computed in Case 4 (*medium mesh;* ridge speed: *0.2 m/s*).

Pipe	Stress (psi)		Stress/F_y	
	Simply Supported Beam	**Fixed Beam**	**Simply Supported Beam**	**Fixed Beam**
Pipe 5	12626.	7828.	0.24	0.15
Pipe 1	14124.	9016.	0.27	0.17
Pipe 13	16262.	9736.	0.31	0.19

Table 6: Maximum bending stress (F_y = 52000 psi) in each of the (fictitious) pipelines located in the top row (see Figure 5) computed in Case 5 (*coarse mesh;* ridge speed: *0.2 m/s*).

Conclusions

We have developed a procedure for CFD modeling of ice-ridge-soil systems by means of a simplified treatment of soil as a viscous fluid. Our ultimate objective is the analysis of complete ridge-soil-pipeline systems in a multiphysics environment where we will combine our CFD model of seabed scour with a finite-element model of the pipeline. We have carried out simulations and reported results for seabed scour and pipeline bending stress, recognizing that our procedure in its present form does not account for soil-pipeline interaction. The results suggest a ridge-speed effect on seabed scour and pipeline bending stress, a possibility that has not received attention in recent studies of ridge-soil-pipeline systems. Furthermore, our simulations, albeit limited, indicate that the maximum bending stress decreases to levels much lower than the typical pipe steel yield stress assumed in our calculations (*52,000 psi*; *359 MPa*) at soil cover of one pipe diameter (*24 in*; *0.61 m*). In the extreme case of no cover (unacceptable for the practical point of view but theoretically possible), the maximum bending stress rises to about twice the assumed yield stress. The minimum pipe thickness that would be required in this extreme case to prevent yielding is rather excessive: about 2.4 in (pipe diameter-to-thickness ratio about 10). On the other hand, as the soil cover increases to one pipe diameter, the minimum pipe-thickness requirement falls sharply to a very low level. It should be kept in mind that these findings correspond to soil yield shear stress of *25 kPa*, scour depth of *1 m* and, in addition, the effects of soil-pipe interaction have not been accounted for.

References:

Ahmaogak, G. (2000). "Offshore Oil Development in the Alaskan Arctic: Who Bears the Risk," *Proceedings,* Second Ice Scour and Arctic Marine Pipelines Workshop, pp. 1-4.

Clark, J.I., Paulin, M.J., Lach, P.R., Yang, Q.S., and Poorooshasb, H.B. (1994). "Development of a Design Methodology for Pipelines in Ice Scoured Seabeds," *Proceedings,* Thirteenth International Conference on Offshore Mechanics and Arctic Engineering, Vol. V, Houston, Texas, pp. 107-125.

Hurley, S., and Phillips, R. (1998). "Safety and Integrity of Arctic Marine Pipelines: Progress Report #2 – Centrifuge Test PR3d-1 Report," *Contract Report for Minerals Management Service,* U.S. Department of the Interior, *C-CORE Publication 98-C2.*

Konuk, I., and Gracie, R. (2004). "A 3-Dimensional Eulerian Finite Element Model for Ice Scour," *Proceedings,* International Pipeline Conference, Calgary, Alberta, October 4-8.

Konuk, I., and Yu, S. (2007). "A Pipeline Case Study for Ice Scour Design," *Proceedings,* 26th International Conference on Offshore Mechanics and Arctic Engineering, San Diego, California, June 10-15.

Kovacs, A., and Mellor, M. (1974). "Sea Ice Morphology and Ice as a Geologic Agent in the Southern Beaufort Sea," *The Coast and the Shelf of the Beaufort Sea,* The Arctic Institute of North America, Arlington, Virginia, pp. 113-164.

Lach, P.R., Clark, J.I., and Poorooshasb, F. (1993). "Centrifuge Modeling of Ice Scour," *Proceedings,* Fourth Canadian Conference on Marine Geotechnical Engineering, Volume 1, St. John's, Newfoundland, pp. 356-374.

Nobahar, A., Kenny, S., and Phillips, R. (2007). "Buried Pipelines Subject to Subgouge Deformations," *International Journal of Geomechanics,* **3**, pp. 206-216.

Palmer, A.C. (1997). "Geotechnical Evidence of Ice Scour as a Guide to Pipeline Burial Depth," *Canadian Geotechnical Journal,* **34**, pp. 1002-1003.

Palmer, A.C. (2000). "Gouging in the Context of Critical Issues for Arctic Offshore Pipeline Development," *Proceedings,* Second Ice Scour and Arctic Marine Pipelines Workshop, pp. 5-10.

Paulin, M.J. (1992). "Physical Model Analysis of Iceberg Scour in Dry and Submerged Sand," *M. Eng. Thesis,* Memorial University of Newfoundland.

Raie, M.S. (2009). "A Computational Procedure for Simulation of Torpedo Anchor Installation, Set-Up and Pull-Out," *Ph.D. Dissertation,* The University of Texas, Austin, Texas.

Schoonbeek, I.S.S., and Allersma, H.G.B. (2006). "Centrifuge Modelling of Scouring Ice Keels in Clay," *Physical Modeling in Geotechnics, Proceedings,* Sixth International Conference, pp. 1291 - 1296.

Winsor, R., and Parsons, G. (1997). "Pressure Ridge Ice Scour Experiment Phase 3c, Extreme Ice Scour Event – Modeling and Interpretation, Milestone 2: Centrifuge Test PRSA02 Data Report," Contract Report for BP Alaska, Chevron Petroleum Technology,

Exxon Production Research Co., Petro-Canada, and Union Texas Petroleum, *C-CORE Publication 97-C6.*

Woodworth-Lynas, C.M.T. (1992). "The Geology of Ice Scour," *Ph.D. Thesis,* University of Wales.

Yang, Q.S., Lach, P.R., Clark, J.I., and Poorooshasb, H.B. (1994). "Comparisons of Physical and Numerical Models of Ice Scour," *Proceedings,* Eighth International Conference on Computer Methods and Advances in Geomechanics, Volume 2, Morgantown, West Virginia, pp. 1795-1801.

Yang, Q.S., and Poorooshasb, H.B. (1997). "Numerical Modeling of Seabed Ice Scour," *Computers and Geotechnics,* **21**, 1, pp. 1-20.